JACS
JOURNAL OF THE AMERICAN CHEMICAL SOCIETY
Article
pubs.acs.org/JACS

Predicting the Electrochemical Behavior of Lithium Nitrite in Acetonitrile with Quantum Chemical Methods

Vyacheslav S. Bryantsev,* Jasim Uddin, Vincent Giordani, Wesley Walker, Gregory V. Chase, and Dan Addison

Liox Power, Inc., 129 N. Hill Ave., Suite 103, Pasadena, California 91106, United States

Supporting Information

ABSTRACT: Electrolyte stability is an essential prerequisite for the successful development of a rechargeable organic electrolyte Li-O_2 battery. Lithium nitrate ($LiNO_3$) salt was employed in our previous work because it was capable of stabilizing a solid-electrolyte interphase on the Li anode. The byproduct of this process is lithium nitrite ($LiNO_2$), the fate of which in a Li-O_2 battery is unknown. In this work, we employ density functional theory and coupled-cluster calculations combined with an implicit solvation model for neutral molecules and a mixed cluster/continuum model for single ions to understand the chemical and electrochemical behavior of $LiNO_2$ in acetonitrile (AN). The redox potentials of oxygenated nitrogen compounds predicted in this study are in excellent agreement with the experimental results (the average accuracy is 0.10 V). Theoretical calculations suggest that the reaction between the nitrite ion and its first oxidation product, nitrogen dioxide (NO_2), in AN solution proceeds via the initial formation of a *trans*-ONO-NO_2 dimer that is subject to autoionization and the subsequent reaction of produced nitrosyl ion (NO^+) with NO_2^-. Good agreement between experimental and simulated cyclic voltammograms for electrochemical oxidation of $LiNO_2$ in AN provides support to the proposed mechanism of coupled electrochemical and chemical reactions. The results suggest a possible mechanism of regeneration of $LiNO_3$ in electrolyte in the presence of oxygen, which is uniquely possible under charging conditions in a Li-O_2 battery.

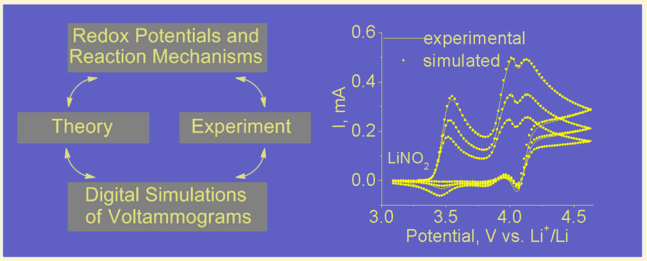

1. INTRODUCTION

As hybrid and full electric vehicles continue to increase in sales and popularity around the world, the race is on to develop batteries that can deliver higher capacities at lower costs. Li-O_2 batteries have been heavily investigated as a potential battery system to replace Li-ion because of a high theoretical specific energy, however research into Li-O_2 cells has been hampered by degradation issues with every major component of the system upon cycling, and progress has been slow.[1−5]

Liquid electrolyte plays a critical role in determining the nature of discharge products and cycling characteristics of a rechargeable Li-O_2 battery. One of the biggest challenges is to develop an electrolyte composition that is sufficiently stable to both the Li anode and O_2 cathode environments upon long-term cycling.[1−5] We have recently reported[6] on the Li-O_2 cell that enables longer duration cycling (>2000 h) with significantly reduced decomposition of electrolyte materials compared to Li-O_2 cells previously reported in the field. This performance is achieved by combining straight-chain alkyl amides, which are significantly more stable to the reactions of the O_2 electrode than conventional electrolyte solvents,[6,7] with the lithium nitrate ($LiNO_3$) salt, which is capable of stabilizing a solid-electrolyte interphase (SEI) on the Li anode.[8−11]

It was suggested[8] that a stabilizing effect of $LiNO_3$ on Li metal cycling is due to the formation of a passivating layer of Li_2O on the Li electrode surface through the following reaction:

$$2Li + LiNO_3 \rightarrow Li_2O + LiNO_2 \quad (1)$$

Another product of this reaction, lithium nitrite ($LiNO_2$), is expected to be soluble and electroactive in the charging potential range of a Li-O_2 cell. Indeed, small oxidative processes at 3.6−3.7 V observed in a Li-O_2 cell with a $LiNO_3$/dimethylacetamide (DMA) electrolyte[6] are consistent with the presence of $LiNO_2$ in an electrolyte solution. $LiNO_3$ is used as an electrolyte additive in rechargeable lithium-sulfur (Li-S) batteries to promote the formation of a stable passivation film on Li anode, which is known to significantly suppress the reduction of polysulfide species in solution.[9,10] However, the progressive consumption of $LiNO_3$ on the Li anode in Li-S batteries limits the number of cycles over which $LiNO_3$ is able to prevent the redox shuttle of lithium polysulfides. We have recently shown[12] that $LiNO_3$ can be regenerated from $LiNO_2$ in the presence of dissolved O_2 during the charging of a Li-O_2 battery, which could be a contributing factor to the observed interfacial stability and cycling of Li metal when both $LiNO_3$ and O_2 are present.[11] Detailed knowledge of the chemical and electrochemical behavior of $LiNO_2$ in aprotic solvents is thus essential to gain further insights into the mechanism of regeneration of NO_3^- in rechargeable Li-O_2 cells.

Received: October 21, 2013
Published: February 3, 2014

   dx.doi.org/10.1021/ja410766n | J. Am. Chem. Soc. 2014, 136, 3087−3096

Table 1. Comparison of the Calculated and Experimental Gibbs Free Energies of Gas-Phase Reactions involving Nitrogen−Oxygen Compounds (kcal/mol)[a]

	B3LYP		M06		M06-L		M06-2X			
reaction	BS1	BS2	BS1	BS2	BS1	BS2	BS1	BS2	RCCSD(T)/CBS	expt[c]
$2NO_2 = N_2O_4$	1.7	1.7	−5.8	−5.8	−5.4	−6.1	−0.7	−1.4	−0.5	−1.1
$NO_2 + NO = N_2O_3$	2.9	2.8	−3.5	−3.2	−6.1	−6.1	3.4	2.5	1.3	0.4
$NO_2^- + NO_2 = NO_3^- + NO$	−12.1	−11.4	−13.0	−12.2	−8.2	−7.9	−19.3	−18.5	−13.9	−14.1
$NO_2^- + 1/2N_2O_4 = NO_3^- + NO$	−12.9	−12.3	−10.0	−9.3	−5.5	−4.9	−18.9	−17.8	−14.0	−13.5
$N_2O_4 = NO^+ + NO_3^-$	159.5	159.9	160.5	160.8	172.7	170.8	147.7	148.2	147.6	149.4
$N_2O_4 = NO_2^+ + NO_2^-$	177.5	175.9	177.1	174.1	182.8	178.1	177.2	175.3	170.4	
$N_2O_3 = NO^+ + NO_2^-$	170.3	170.1	171.1	170.4	181.5	178.8	162.9	162.8	160.4	161.9
$2NO + O_2 = 2NO_2$	−18.6	−19.9	−28.1	−28.6	−33.2	−33.9	−8.9	−12.3	−16.7	−16.9
$2NO_2 + 1/2O_2 = N_2O_5$	11.0	9.8	−0.04	−0.54	3.6	2.3	4.4	2.6	3.0	3.70
MUE, RCCSD(T)/CBS[b]	5.1	5.1	6.6	6.5	11.4	10.6	3.5	2.6	0.8	
MUE, expt[b]	4.4	4.6	6.1	6.3	10.5	10.4	3.2	2.4		

[a]BS1 is the 6-311+G* basis set. BS2 is the aug-cc-pVTZ basis set. Geometries were optimized at each basis set and density functional. Zero point energies and thermal corrections were calculated at the B3LYP/6-311+G* level. [b]MUE versus benchmark calculations at the RCCSD(T)/CBS level and experiment. [c]Ref 46.

The electrochemical oxidation of the oxygenated nitrogen compounds has been studied previously in various media, but the reported results are often inconsistent.[12−22] For example, the redox potential of the NO_2/NO_2^+ couple was reported to vary by more than 0.6 V in the same solvent.[18,21] This ambiguity was assigned to the problem of contamination by traces of water that can react with nitrogen oxides to generate new electroactive species.[21] Due to lack of detailed mechanistic understanding of nitrite oxidation, there are significant contradictions and variations in the interpretation of the successive oxidation waves of the nitrite anion.[12,13,16,19,20,22]

In this work, we employ theoretical calculations to predict redox potentials of oxygenated nitrogen compounds in acetonitrile (AN) solution. AN is chosen as a solvent in this study because similarly to straight-chain alkyl amides, it shows improved stability toward reduced O_2 species[7] but offers a wider electrochemical window, thus extending the range of accessible redox potentials. Ion solvation is modeled by explicit inclusion of eight solvent molecules in the vicinity of the ion and implicit treatment of the rest of the solvent with a dielectric continuum model. This mixed cluster/continuum framework[23,24] avoids the ambiguities of assigning atomic O and N radii for ionic compounds, because the results are not sensitive to the choice of these parameters if a solute is completely surrounded by solvent molecules. Excellent agreement with the experimental redox potentials provides strong support for the computational model, thereby lending credence to the calculated solvation free energies of various ionic nitrogen−oxygen species. Furthermore, we have investigated the mechanism of the chemical reaction between the nitrite anion and its first oxidation product, nitrogen dioxide (NO_2) and its dimer. We find that the interconversion between nitrogen dioxide and its various dimers provides a low-energy path for the reaction with the nitrite anion. Good agreement between experimental and simulated cyclic voltammograms for electrochemical oxidation of $LiNO_2$ in AN provides support to the proposed mechanism of coupled electrochemical and chemical reactions. The results have important practical consequences for rechargeable Li-O_2 batteries, suggesting a possible mechanism of regeneration of $LiNO_3$ in the electrolyte. In a more general context, first principles calculations can now provide valuable insight into solution-phase chemistry and open new opportunities for the use of theory in elucidating mechanisms of electrochemical processes in organic media and guiding the assignment of the cyclic voltammetry peaks.

2. COMPUTATIONAL METHODS

2.1. Gas-Phase Calculations. We used the restricted open-shell second-order Möller−Plesset perturbation theory (MP2)[25,26] in the complete basis set (CBS) limit and coupled-cluster theory with singles, doubles, and perturbative triples excitations for restricted reference wave functions (RCCSD(T))[26−29] in the aug-cc-pVnZ (n = D and T) basis set[30,31] to determine the benchmark reaction energies and barriers involving oxygenated nitrogen compounds. Only the valence electrons were correlated in the RMP2 and RCCSD(T) calculations. Assuming that the difference between RCCSD(T) and RMP2 energies exhibits only a small basis set dependence, the RCCSD(T) energies at the CBS limit can be estimated as[32]

$$\Delta E(\mathrm{RCCSD(T)/CBS}) = \Delta E(\mathrm{RMP2/CBS}) + \delta\mathrm{RCCSD(T)} \quad (2)$$

$$\delta\mathrm{RCCSD(T)} = \Delta E(\mathrm{RCCSD(T)/aug\text{-}cc\text{-}pVnZ}) - \Delta E(\mathrm{RMP2/aug\text{-}cc\text{-}pVnZ}) \quad (3)$$

Test calculations for the NO_2 dimer show that the δRCCSD(T) corrections vary by 0.67 and 0.20 kcal/mol upon extending the basis set aug-cc-PVnZ from n = D to T and T to Q, respectively. Thus, the combination of RMP2/CBS with RCCSD(T)/aug-cc-pVTZ corrections provides an excellent compromise between accuracy and computational cost. The geometries of nitrogen−oxygen compounds in all post-Hartree−Fock calculations were obtained at the RCCSD(T)/aug-cc-pVDZ level. Minimization and transition-state optimization was performed using the Driver module of NWChem[26] with default convergence criteria. The binding energy for the NO_2 dimer differs by only 0.05 kcal/mol when compared to results obtained after full optimization at the RCCSD(T)/aug-cc-pVTZ level. However, if the geometry is obtained at the RMP2/aug-cc-pVDZ level, the binding energy for the NO_2 dimer from single-point calculations at the RCCSD(T) level is underestimated by ∼1 kcal/mol. For the basis set expansion in our RMP2 calculations, we used a family of Dunning's[30,31] augmented correlation-consistent basis sets up to quadruple-

dx.doi.org/10.1021/ja410766n | J. Am. Chem. Soc. 2014, 136, 3087−3096

and quintuple-ζ quality with spherical harmonic functions. All RMP2 and RCCSD(T) calculations were carried out using the NWChem 5.1 program package.[26]

It was shown by Liu and Goddard[33] that the choice of the reference wave function in coupled-cluster calculations has a significant effect on the potential energy surface for the dimerization of NO_2. In agreement with this work[33] we found that the restricted wave function method, RCCSD(T), recovers more correlation energy near the equilibrium bond distance than does the unrestricted wave function method and gives a more reliable estimate for the binding energy of the NO_2 dimer.

We examined the ability of B3LYP[34,35] and a family of M06 density functionals (M06, M06-L, and M06-2X)[36,37] in the unrestricted spin formalism to reproduce the benchmark RCCSD(T) binding and reaction energies involving oxygenated nitrogen compounds. The proper open-shell initial guess was necessary for several NO_2 dimer geometries (open-shell singlet state).[33] Using a closed-shell initial guess can bias the solution toward the closed-shell state with higher energy. For each of these functionals, two basis sets were considered: 6-311+G* (one set of polarization d-funtions; for systems containing H atom the basis set was 6-311++G**) and aug-cc-pVTZ. The ultrafine numerical integration grid was employed in all DFT calculations. The B3LYP functional was chosen to calculate the free energy barriers for the reaction of NO_2^- with NO_2 and N_2O_4, based on adequate description of thermodynamic data for these reactions (Table 1). Additionally, B3LYP calculations showed reasonable agreement with RCCSD(T)/CBS potential energy surfaces for interconversion between NO_2 and its dimers.[33] A transition-state search with the B3LYP method was performed using a standard quasi-Newton method in Jaguar,[38] starting from the partially optimized geometry at the same level of theory along the chosen reaction coordinate and the precalculated Hessian. For transition states, one single imaginary frequency at the B3LYP/6-311+G* level was obtained in all cases, which upon visualization was found to correspond to the expected motion along the reaction coordinate. Additionally, intrinsic reaction coordinate calculations (IRC) were performed at the B3LYP/6-311+G* level (as implemented in Jaguar)[38] to ensure that transition-state structures connect their respective reactants and products. Structural features of the transition states connecting NO_2 and its dimers are in agreement with previous work.[33] The standard Gibbs free energy of each species in the gas phase (T = 298 K, P = 1 atm) was calculated using the rigid rotor-harmonic oscillator approximation without scaling, except that vibrational frequencies lower than 50 cm^{-1} were raised to 50 cm^{-1}. This procedure is similar to that proposed by Truhlar and co-workers[39] as a way to correct for the well-known breakdown of the harmonic oscillator model for the free energies of low-frequency vibrational modes.

2.2. Implicit Solvation Calculations. Solvation calculations were carried out using the Poisson−Boltzmann continuum model in Jaguar[38] for the AN solvent, characterized by a dielectric constant of 35.97 and the probe radius of 2.180. The electronic energies in the solvent reaction filed were obtained at the B3LYP/6-311+G* levels. Using the default solute van der Waals radii in Jaguar leads to a systematic overestimation of the solvation free energy for polar solutes in AN.[24] To obtain the optimal performance for polar solvents if only the electrostatic contribution to the solvation free energy is included, the default values of solute atomic radii were scaled by 1.20. This description combined with RCCSD(T)/CBS results gives reasonable values of Gibbs free energies for $2NO_2 = N_2O_4$ (−4.9 kcal/mol) and $NO_2 + NO = N_2O_3$ (−3.7 kcal/mol) in AN (the deviation from experiment[20,40] is 1.3 and 1.9 kcal/mol, respectively).

2.3. Configurational Sampling of Solute−Solvent Clusters. A search of the low-energy solute−solvent clusters was performed using the Monte Carlo sampling algorithm (called BLENDS)[41,42] to generate 40 initial cluster configurations. Some initial configurations were also built upon visual inspection and manual rearrangement of the optimized clusters. The initial structures were subjected to full geometry optimization at the B3LYP/6-31G** level, followed by single point energy calculations at either M06-L/6-311++G** or M06-2X/6-311++G** level (see Section 4.3). These were combined with the implicit solvation free energies computed at the B3LYP/6-311++G** level to yield the final ranking of the clusters. Pure AN clusters were taken from our previous study.[24]

3. EXPERIMENTAL SECTION

3.1. General. Anhydrous AN (99.8%) was purchased from Sigma-Aldrich and used as received. Lithium nitrite ($LiNO_2$) was synthesized in our lab according to the procedure described previously.[12] $LiNO_3$ (Sigma Aldrich, ≥99.5%) and LiTFSI (Novolyte) were dried at 200 °C for 3 days under vacuum prior to use. Nitronium tetrafluoroborate ($NOBF_4$, >95%) was purchased from Sigma Aldrich. All electrolytes had a final water content <10 ppm as determined by Mettler Toledo Karl Fischer titration. Li rod for reference electrode was purchased from Alfar Aesar and washed with hexane before used. Ultra-high-purity argon and O_2 gases (Airgas) were used for purging the electrolyte. NO_2 gas (Sigma Aldrich, ≥99.5%) was used as received. The UV−vis spectrometry measurements were performed using a Perkin-Elmer Lambda 25 Spectrometer with quartz SUPRASIL cells. Mass spectrometry measurements were made with a Stanford Research Systems RGA100 (1−100 amu) residual gas analyzer attached to high-vacuum system (1×10^{-8} Torr) from Pfeiffer Vacuum.

3.2. Cyclic Voltammetry. The cyclic voltammetry (CV) experiments were performed with a VMP3 (BioLogic Science Instruments) potentiostat. The electrochemical cell (Pine Instrument Company) is constructed in a dry glovebox. The cell consisted of a traditional three electrode system utilizing a Li-rod reference electrode salt-bridged in an electrolyte containing 5 M LiTFSI in AN. The lithium reference electrode potential was converted to the Li^+/Li potential scale using the Nernst equation. A platinum wire was used as the counter electrode in a fritted compartment, and a platinum disk (0.196 cm^2) was used as working electrode, which was polished with 0.05 mm alumina paste prior to each experiment. Cyclic voltammetric data indicate that the 0.5 M LiTFSI in AN has high anodic stability (>5.0 V versus Li^+/Li). The accessible redox potentials are within the range exhibited by oxygenated nitrogen compounds. Digital simulations were conducted with DigiElch,[43] version 6.F, a software package for the digital simulation of common electrochemical experiments.

3.3. Reaction of NO_2/N_2O_4 with $LiNO_2$. The reaction between NO_2/N_2O_4 and $LiNO_2$ in AN was carried out in the dry glovebox under argon. NO_2 gas was condensed to N_2O_4 at −78 °C in a sealed tube, and then AN was added to make a NO_2/N_2O_4 solution. A portion of solution was placed in a sealed flask under argon, and 21 mM $LiNO_2$ was slowly added into it. A colorless gas evolved immediately upon addition of $LiNO_2$. The gas from the reaction of NO_2/N_2O_4 with $LiNO_2$ was identified as NO by a residual gas analyzer (RGA). The formation of NO_3^- was confirmed by UV−vis analysis (further experimental details are given in the Supporting Information).

4. RESULTS AND DISCUSSION

The electrochemistry of NO_2^- within the charging potential range of the O_2 electrode in Li-O_2 batteries was extensively studied by means of CV in several aprotic organic solvents under inert atmosphere.[16,19,20] In AN[16] and sulfolane[19,20] the voltammetric curves show three consecutive oxidation and two reduction waves. The unambiguous interpretation of the anodic and cathodic waves, however, remains difficult because of the nature of the electrochemical mechanism comprising complex sequences of electrochemical and chemical steps[13,16,19−22] and complications resulting from the presence of water at trace levels.[19,21] In particular, there is no consensus on the origin of the third anodic wave[16,19] and the mechanism of a fast chemical reaction between nitrite and its first oxidation product, NO_2/N_2O_4[16,19,21]

$$NO_2^- + 1/2N_2O_4/NO_2 \rightarrow NO + NO_3^- \quad (4)$$

Furthermore, there are serious discrepancies among several measurements of relative redox potentials of oxygenated nitrogen compounds in aprotic solvents.[18,21] In the following discussion we will show that with a good choice of computational methods in the gas phase and in solution, first principles computations can predict quantitatively correct redox potentials, provide useful mechanistic insights into reaction mechanisms, and with the use of digital simulations[43] of CVs can resolve existing controversies in the interpretation of the electrochemical behavior of NO_2^-. The results suggest a possible mechanism of regeneration of $LiNO_3$ in electrolyte in the presence of oxygen, which may explain the positive synergistic effect of $LiNO_3$ and O_2 in enabling long-term cycling of Li metal.[11]

4.1. Database of Accurate Reaction Energies. The ability of first-principles computational methods to provide sufficiently reliable results to the level at which they can complement and guide the experimental measurements is contingent upon accurate thermodynamic description of reaction processes in the gas phase and in solution. As a benchmark for determining the accuracy of different DFT functionals in the gas phase, we employed reaction and binding energies obtained at the CBS limit of the RCCSD(T) theory (Table S1). The compiled database consists of 9 reaction and 5 complexation energies involving oxygenated nitrogen compounds and 8 reaction/activation energies for interconversion between NO_2 and its dimers.

We find that the RMP2 reaction energies are well converged with respect to the basis set size at the aug-cc-pV5Z level (see Table S1). The inclusion of a higher order of electron correlation at the RCCSD(T) level has resulted in some dramatic changes of the calculated reaction energies and barriers compared to the RMP2 results. The magnitude of the δRCCSD(T) correction is >7 kcal/mol in about one-third of reactions shown in Table S1 and >10 kcal/mol in the most difficult cases involving NO_2 radical. Reactions involving interaction of multicenter free radicals (such as NO_2) require great care because of their high sensitivity to both static and dynamic correlation effects.[33] MP2 method is the first step in going beyond Hartree−Fock that often performs quite well for closed-shell systems. However, for reactions involving the transition between closed- and open-shells, neither RMP2 nor UMP2 is reliable.[33] While, in principle, the use of the multireference wave functions naturally accounts for the static correlation, satisfactory description of dynamic correlation effects could be computationally very demanding. The RCCSD(T)/CBS method offers a good compromise between accuracy and computational cost, because it incorporates the dynamic correlation quite well and provides accurate results for bound molecules and transition-state geometries that are far from the dissociation limit. Based on extended benchmark studies of coupled-cluster theory,[44,45] we expect the database of RCCSD(T)/CBS reaction energies to have an accuracy of 1.0 kcal/mol or better and thus serve as a reliable benchmark for the use of theory in describing the electrochemical processes and evaluating the reliability of more approximate methods.

4.2. The Accuracy of DFT Calculations in the Gas Phase. The RCCSD(T)/CBS reaction energies collected in the previous section enable us to evaluate the reliability of several density functionals for oxygenated nitrogen compounds. Table 1 compares the performance of the B3LYP, M06, M06-L, and M06-2X density functionals with the 6-311+G* and aug-cc-pVTZ basis sets for predicting the Gibbs free energies of reactions involving oxygenated nitrogen compounds (ΔG_r^o). The accuracy of each method is characterized by the mean unsigned error (MUE) versus RCCSD(T)/CBS and experiment.[46]

The RCCSD(T)/CBS calculations yield results that fall within the experimental uncertainty[46] of ΔG_r^o. We note that none of the employed DFT methods provides a completely satisfactory description of reaction energies of oxygenated nitrogen compounds. Among them, the M06-2X and B3LYP functionals significantly outperform the RMP2 method and provide the best overall performance. M06-2X is the most accurate functional for describing the autoionization energies of N_2O_4 and N_2O_3, while B3LYP does a good job in reproducing the thermodynamics for the reaction of NO_2^- with NO_2 and N_2O_4. Based on this performance, selective DFT methods were employed where RCCSD(T)/CBS calculations were not feasible.

4.3. Calculations of Solvation Free Energies of NO^+, NO_2^+, NO_2^-, and NO_3^- in AN. The capability of theoretical models to accurately predict redox potentials without the use of empirical fitting parameters relies upon their ability to accurately describe the solvation free energies of ions. Pure dielectric continuum models are not sufficiently reliable for predicting single-ion solvation free energies. In this work we employ a mixed cluster/continuum approach[23,24] for calculating absolute solvation free energies of single ions, where the most important solute−solvent interactions are included explicitly in the quantum chemical description, while the solvent effects beyond the first solvation shell are described using a dielectric continuum model. From the thermodynamic cycle shown in Figure 1, the solvation free energy of $X^{m\pm}$, $\Delta G^*_{solv}(X^{m\pm})$, can be expressed as the algebraic sum of the gas-phase complexation free energy ($\Delta G^o_{g,bind}$), the difference in the solvation free energy for $[X(solvent)_n]^{m\pm}$ and $(solvent)_n$ clusters calculated

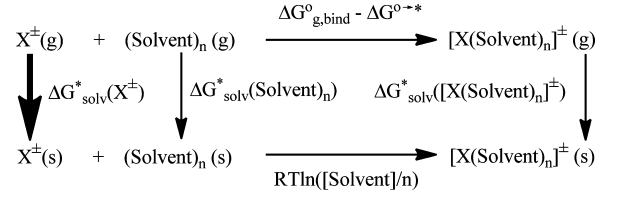

Figure 1. Thermodynamic cycle for the calculation of $\Delta G^*_{solv}(X^{\pm})$.

dx.doi.org/10.1021/ja410766n | J. Am. Chem. Soc. 2014, 136, 3087−3096

using a dielectric continuum model, and the standard state/concentration correction terms[23,47] as described below:

$$\Delta G^{*}_{solv}(X^{m\pm}) = \Delta G^{o}_{g,bind} + \Delta G^{*}_{solv}([X(solvent)_n]^{m\pm}) - \Delta G^{*}_{solv}(solvent)_n - \Delta G^{o\rightarrow *} - RT\ln([solvent]/n) \quad (5)$$

For the correct construction of the thermodynamic cycle, each reactant and product in the upper and lower legs of the cycle must be in the same standard state.[23] The conversion from an ideal gas standard state of 1 atm (24.46 L mol^{-1}) to an ideal solution standard state of 1 M (1 mol L^{-1}) is defined by[47]

$$\Delta G^{o\rightarrow *} = RT\ln(24.46) = 1.89 \text{ kcal/mol } (T = 298.15K) \quad (6)$$

Similarly, $RT\ln([solvent]/n)$ is defined as the free energy change of 1 mol of $(solvent)_n$ ideal gas from $[solvent]/n$ M liquid state to 1 M,[23] where [solvent] is molarity of solvent, and n is the number of solvent molecules in a cluster.

The two most important considerations with mixed cluster/continuum models are the size of the explicit solvation shell and the choice of the DFT method for describing the solute–solvent interactions. Explicit modeling of the first solvation shell for neutral and singly charged solutes was found to be sufficient to give a satisfactory description of their thermodynamic properties in solution.[23,24] Following our previous work on solvation of O_2^- and neutral lithium–oxygen compounds in AN,[24] the inclusion of eight solvent molecules was deemed sufficient to provide a reasonable saturation of the first solvation shell around small inorganic ions. As for the choice of the accurate density functional for noncovalent interaction, we examined the ability of several DFT methods to reproduce the CCSD(T)/CBS binding energies of small ions with the AN dimer. The results, Table 2, indicate that the M06-L density

Table 2. The Accuracy of Several DFT Methods for Predicting the Binding Energies between the AN Dimer and NO^+, NO_2^+, NO_2^-, and NO_3^- Ions in the Gas Phase (kcal/mol)

	DFT/6-311++G**//B3LYP/6-311++G**				
reaction	B3LYP	M06	M06-L	M06-2X	CCSD(T)/CBS
$2AN = (AN)_2$	−4.15	−6.14	−5.94	−6.33	−6.40
$NO^+ + (AN)_2 = NO^+(AN)_2$	−52.38	−51.93	−56.19	−46.68	−43.48
$NO_2^+ + (AN)_2 = NO_2^+(AN)_2$	−44.09	−44.62	−44.01	−45.89	−42.79
$NO_2^- + (AN)_2 = NO_2^-(AN)_2$	−22.58	−23.73	−24.44	−23.10	−22.25
$NO_3^- + (AN)_2 = NO_3^-(AN)_2$	−20.53	−21.65	−22.04	−21.64	−21.24

functional employed in our previous work[24] to model the complexation of Li^+ and O_2^- with AN does a good job in reproducing the interaction energies for NO_2^+, NO_2^-, and NO_3^- but strongly overbinds for the NO^+ ion. M06-2X is the only functional that gives a reasonable estimation of the binding energy between NO^+ and $(AN)_2$. Thus, based on the evaluation of several DFT methods, M06-2X was utilized to model the solvation of the NO^+ ion, while M06-L was employed to model the solvation of NO_2^+, NO_2^-, and NO_3^- ions.

The structures of the most stable $X(AN)_8$ clusters (X = NO^+, NO_2^+, NO_2^-, NO_3^-) used to calculate ion solvation free energies (ΔG^{*}_{solv}) are shown in Figure 2. The protocol for the configurational sampling of solute–solvent clusters is described

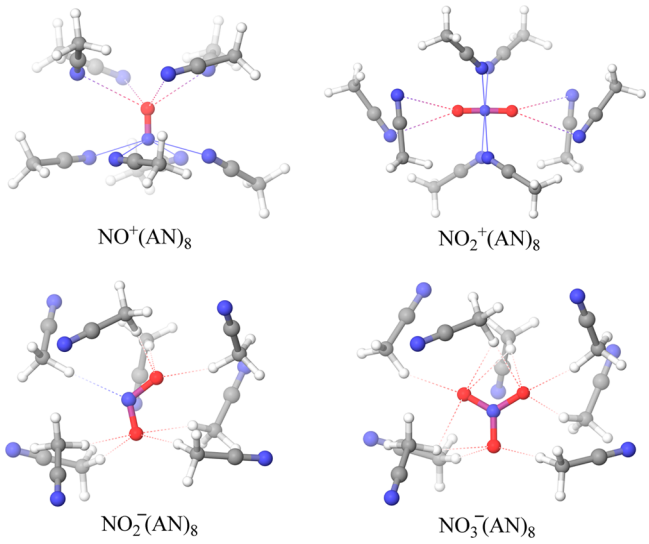

Figure 2. Structures of the $X(AN)_8$ clusters (X = NO^+, NO_2^+, NO_2^-, NO_3^-) optimized at the B3LYP/6-31G** level.

in Section 2.3. The solvation free energies computed using mixed cluster/continuum and pure dielectric continuum model are listed in Table 3. The results of implicit solvation

Table 3. Solvation Free Energies of NO^+, NO_2^+, NO_2^-, and NO_3^- Ions in AN Calculated Using the Mixed Cluster/Continuum and Pure Dielectric Continuum Solvent Models (kcal/mol)

		dielectric continuum model	
ΔG^{*}_{solv}	cluster/continuum model[a]	default[b]	scaled[c]
NO^+	−80.8	−91.5	−77.0
NO_2^+	−77.5	−88.3	−73.7
NO_2^-	−61.4	−71.8	−65.4
NO_3^-	−59.7	−68.4	−61.1

[a]Using the thermodynamic cycle shown in Figure 1. The structures of the ion-$(AN)_8$ clusters employed in these calculations are depicted in Figure 2. [b]Default solute van der Waals radii in Jaguar ($r_O = r_N = 1.60$ Å). [c]van der Waals radii for O and N in Jaguar scaled by a factor 1.2 ($r_O = r_N = 1.92$ Å).

calculations are highly dependent on the choice of atomic radii that define the solute–solvent boundary, which are typically optimized for neutral organic molecules in water. Using the default solute radii in Jaguar leads to a significant overestimation (on average by ~10 kcal/mol) of ΔG^{*}_{solv} for all ions. In this work, the default solute radii are scaled by 1.20 to improve the accuracy of solvation calculations for small neutral molecules in AN. Using a single scaling factor also helps to improve the calculated ΔG^{*}_{solv} for ions, which are now in much better agreement with the values obtained using the mixed cluster/continuum model. However, even with the optimized scaling parameter, the implicit solvation calculations overestimate ΔG^{*}_{solv} for anions and underestimate ΔG^{*}_{solv} for cations (Table 3).

4.4. Calculations of Redox Potentials of Nitrogen Oxides in AN. Redox potentials versus Li^+/Li scale are calculated using the thermodynamic cycle shown in Figure 3. In

dx.doi.org/10.1021/ja410766n | J. Am. Chem. Soc. 2014, 136, 3087–3096

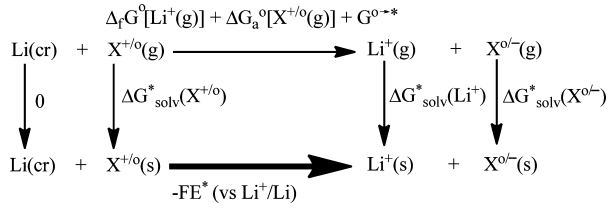

Figure 3. Thermodynamic cycle for the calculation of redox potentials versus Li^+/Li scale.

this cycle, $\Delta_f G^o[Li^+(g)]$ is the standard gas-phase free energies of formation of Li^+, $\Delta G_a^o[X^{+/o}(g)]$ is the electron attachement free energy of $X^{+/o}(g)$, F is Faraday's constant, E^* is the standard reduction potential vs Li^+/Li, ΔG^*_{solv} is the solvation free energy of Li^+, $X^{+/o}$, and $X^{o/-}$ ($X^{o/-}$ = NO_2^-, NO, NO_2, NO_3^-), and $\Delta G^{o\rightarrow *}$ is defined by eq 6. Through the use of the thermodynamic cycle in Figure 3, we can write

$$-FE^*(\text{vs } Li^+/Li) = \Delta_f G^o[Li^+(g)] + \Delta G_a^o[X^{+/o}(g)] + \Delta G^{o\rightarrow *} + \Delta G^*_{solv}(Li^+) + \Delta G^*_{solv}(X^{o/-}) - \Delta G^*_{solv}(X^{+/o}) \quad (7)$$

The superscript asterisk is used to underline that the electrode potential refers to a 1 M ideal solution. Substituting the tabulated[46] value for $\Delta_f G^o[Li^+(g)]$ (154.59 kcal/mol) and $\Delta G^{o\rightarrow *}$ (1.89 kcal/mol) into eq 7, together with the value of $\Delta G^*_{solv}(Li^+)$ (−121.7 kcal/mol) calculated using the explicitly solvated $Li^+(AN)_4$ cluster, we obtain

$$E^*(\text{vs } Li^+/Li) = -1.51(V) - (\Delta G_a^o[X^{+/o}(g)] + \Delta G^*_{solv}(X^{o/-}) - \Delta G^*_{solv}(X^{+/o}))/F \quad (8)$$

The calculations of E^* reported here are based on accurate values of $\Delta G_a^o[X^{+/o}(g)]$ obtained from RCCSD(T)/CBS calculations and our best estimates of $\Delta G^*_{solv}(X^{\pm})$ derived from mixed cluster/continuum calculations (the second column of Table 3). CV was used to approximate the redox potential of NO_2/NO_2^- and NO^+/NO couples. If a redox process involves oxidation or reduction of a gas, a voltage correction for gas solubility in the units of M/bar was applied in order to make a proper comparison of the measured redox potentials derived from CV with computed ones based on quantum chemical calculations (see ref 48 for a more thorough discussion). At low $LiNO_2$ and $LiNO_3$ concentrations (10 mM), it is reasonable to assume that the two ions are well separated and can be very well modeled as "free" ions.

Table 4 shows a comparison of the calculated and experimental redox potentials of oxygenated nitrogen compound in AN. Overall, our computational protocol is capable of accurately predicting the redox potentials of oxygenated nitrogen compounds in AN solution, with the maximum error and MUE of only 0.13 and 0.10 V, respectively. Among the DFT methods (Table S2), the M06 density functional with the MUE of 0.17 V shows the best overall performance and thus can be recommended to calculate electron-transfer energies in cases where the RCCSD(T) method is not feasible. It is important to note that no adjustable parameters were employed in these calculations. In contrast, a close agreement between computed and experimentally determined redox potentials would not be possible with pure dielectric continuum solvent models without the use of empirical fitting parameters.

Previous results showed some ambiguity regarding the electrochemical behavior of NO^+ and NO_2^+ ions. The work by Lee at al.[18] suggested that the reduction of NO^+ is taking

Table 4. Comparison of Calculated and Experimental Redox Potentials for Oxygenated Nitrogen Compounds in AN (vs Li^+/Li, V)

half-reaction	calcd[a]	expt
$NO_2 + e \rightleftharpoons NO_2^-$	3.44	3.50[b]
$NO^+ + e \rightleftharpoons NO$	4.30	4.17[c]
$NO_2^+ + e \rightleftharpoons NO_2$	4.84	~4.77[d]
$NO_3 + e \rightleftharpoons NO_3^-$	5.07	~4.95[e]

[a]Using the thermodynamic cycle shown in Figure 3. Electron attachment/detachment energies are obtained at the RCCSD(T) level. Zero point energies and thermal corrections are obtained at the B3LYP/6-311+G* level. [b]Obtained from the simulated CVs for the oxidation of 10 mM $LiNO_2$ under Ar and corrected for the ~30 mM/bar solubility[18] of NO_2 in AN. [c]Determined from the CV experiments for 10 mM $NO^+BF_4^-$ (Figure S4) and corrected for the ~10 mM/bar solubility[17] of NO in AN. [d]Estimated from the reported[21] difference of 0.60 ± 0.10 V in standard potentials between the NO_2^+/NO_2 and NO^+/NO couples in several solvents. [e]Estimated from the anodic peak current potential in the CV experiments for 10 mM $LiNO_3$ at a scan rate of 100 mV/s.

place in the same oxidation potential range as that of NO_2^+, while the study by Boughriet et al.[21] found that the oxidizing character of NO_2^+ ions is much higher (by 0.6 ± 0.1 V) than that of NO^+ ions. Our calculated difference in the redox potentials of NO^+/NO and NO_2^+/NO_2 couples (0.54 V) agrees closely with the results of Boughriet et al.[21] We therefore concur with their conclusion that the disparate results found by Lee et al.[18] are due to problems of solvent contamination by traces of water, which promote the conversion of NO_2^+ to NO^+.

4.5. Mechanistic Insights into the Reaction Between NO_2^- and NO_2/N_2O_4 in AN. There is direct experimental evidence that the reaction between NO_2^- and NO_2/N_2O_4 in AN to form NO and NO_3^- is very fast on the time scale of the CV experiments (reaction 4). However, there is a lack of fundamental understanding of the underlying mechanism that drives this reaction. Quantum chemical calculations were carried out to estimate various reaction pathways for the overall reaction 4.

In many reactions with protic substrates, it is not the NO_2 monomer itself, but its asymmetric dimer, ONO-NO_2, that is considered to be the active species.[33] The explanation for the enhanced reactivity of ONO-NO_2 lies in its ability to autodissociate and to generate strongly oxidizing nitrosyl (NO^+) ions. Assuming a very fast reaction between oppositely charged NO^+ and NO_2^- ions, we might similarly expect ONO-NO_2 to directly participate in the reaction with NO_2^-. To test this hypothesis, we studied the interconversion between NO_2 and its dimers at the RCCSD(T)/CBS level, with solvation effects included through the polarizable continuum mode (Figure 4). We note that the mechanism presented here is qualitatively similar to the gas-phase mechanism suggested by Liu and Goddard.[33] All stationary points obtained previously at the B3LYP level[33] were refined at the RCCSD(T)/aug-cc-pVDZ level of theory.

A *trans* form of ONO-NO_2 is expected to be more prone to autodissociation, because it is reported to provide a low-energy pathway for exchange of NO^+ between oxygen atoms in NO_3^-. A direct transformation $2NO_2 \rightarrow$ *trans*-ONO-NO_2 is associated with an activation energy of 21.8 kcal/mol. Following the work of Liu and Goddard,[33] we have also found a low energy reaction path from the two NO_2 monomers to the *trans*-ONO-NO_2

dx.doi.org/10.1021/ja410766n | J. Am. Chem. Soc. 2014, 136, 3087−3096

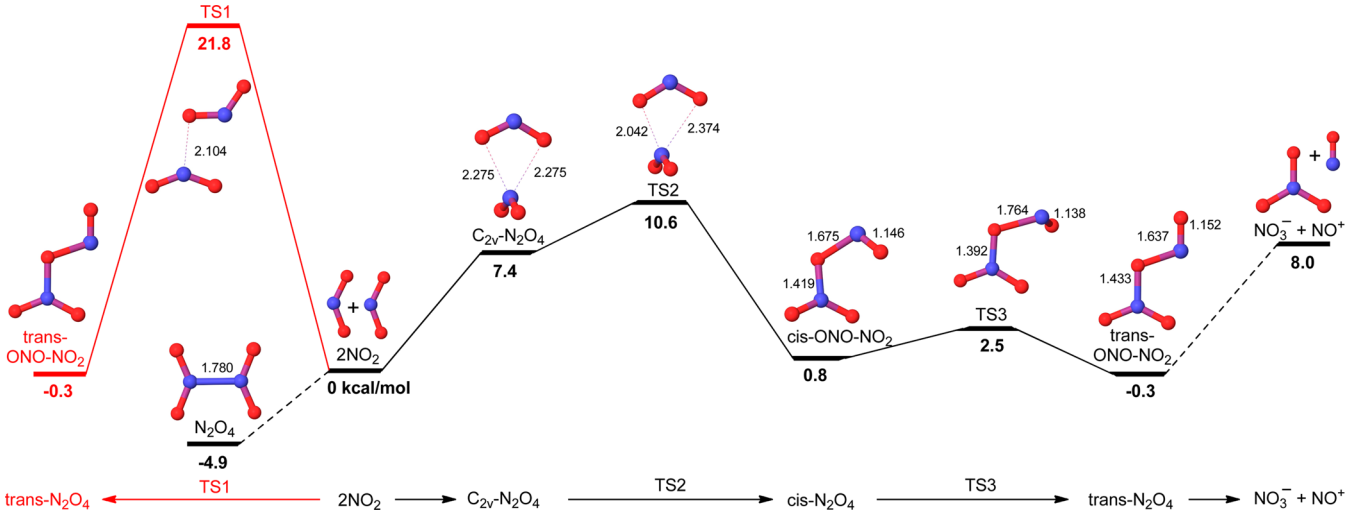

Figure 4. Reaction free energy profile for interconversion between NO_2 and its dimers. Energies are estimated at the CCSD(T)/CBS level with solvation effects included through the polarizable continuum model. CCSD(T)/aug-cc-pVTZ-optimized bond distances are shown in Å.

dimer, which consists of the following steps: $2NO_2 \rightarrow C_{2v}$-$N_2O_4 \rightarrow$ *cis*-ONO-$NO_2 \rightarrow$ *trans*-ONO-NO_2. The transition state for the rate-determining step (TS2), C_{2v}-$N_2O_4 \rightarrow$ *cis*-ONO-NO_2, lies only 10.6 kcal/mol above the two NO_2 monomers or 15.5 kcal/mol above the most stable symmetric N_2O_4 dimer. Furthermore, the autodissociation of *trans*-ONO-NO_2 in the presence of NO_2^- is found to be barrierless, suggesting that the reaction barrier for *trans*-ONO-$NO_2 \rightarrow NO^+ + NO_3^-$ is essentially determined by the thermodynamic stability of reaction products. The low-energy pathway for interconversion between NO_2 monomers and *trans*-ONO-NO_2 is in accordance with a relatively high rate observed for reaction 4. Conversely, the reaction pathway involving the direct oxygen transfer from either NO_2 or symmetric N_2O_4 dimer (D_{2h}) to NO_2^- requires much higher activation energy (>25 kcal/mol), and therefore it is not supported by our calculations (Figures S1 and S2).

4.6. Electrochemical Oxidation of Lithium Nitrite ($LiNO_2$) in AN: A Comparison of Experimental and Simulated Cyclic Voltammograms. Based on the computational results presented in the preceding sections, we can provide a mechanistic analysis of electrochemical oxidation of NO_2^-. To verify the validity of a given mechanism of coupled electrochemical and chemical reactions in AN, the one-dimensional simulation program DigiElch 6.F[43] was used to model the CVs of 10 mM $LiNO_2$ on a Pt macroelectrode under inert atmosphere at scan rates of 50, 100, and 200 mV/s. To evaluate how the formation of various NO_2 dimers influences the electrochemistry of NO_2^- in AN, two reactions scheme of different degrees of complexity were considered.

The basic reaction scheme comprises the following electrochemical and chemical steps (model 1, reactions 9–12):

$$NO_2 + e \rightarrow NO_2^- \quad (9)$$

$$NO_2 + NO_2 \rightleftharpoons [N_2O_4] \rightleftharpoons NO^+ + NO_3^- \quad (10)$$

$$NO_2^- + NO^+ \rightarrow NO_2 + NO \quad (11)$$

$$NO^+ + e \rightarrow NO \quad (12)$$

The voltammograms of $LiNO_2$ in AN under argon show three distinct anodic and two cathodic waves (Figure 5). The

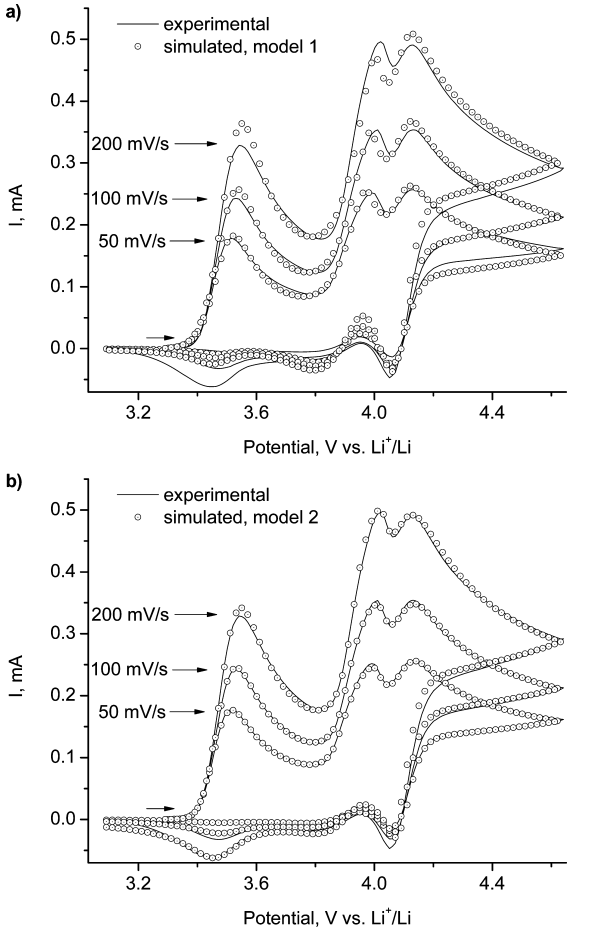

Figure 5. Comparison of experimental and simulated the first scan cyclic voltammograms for the oxidation of 10 mM $LiNO_2$ in 0.5 M LiTFSI/AN electrolyte on a Pt macroelectrode (d = 5 mm) at scan rates of 50, 100, and 200 mV/s. Cyclic voltammograms are shown after subtracting the background current and full IR compensation. Digital simulation of the CV curves based on (a) reactions 9–12 (model 1) and (b) reactions 9, 11, 12, and 14–19 (model 2).

anodic peak at ~3.5 V vs Li^+/Li is assigned to electrode reaction 9, followed by a series of rapid chemical reactions 10

dx.doi.org/10.1021/ja410766n | J. Am. Chem. Soc. 2014, 136, 3087–3096

and 11. In this mechanism, the nitrite oxidation product, NO_2, undergoes dimerization and subsequent autoionization to form NO^+ and NO_3^- ions. The ionic recombination ultimately enables the conversion of NO_2^- into equimolar mixture of NO_3^- and NO during the first oxidation wave (the sum of reactions 9−11)

$$NO_3^- + NO + e \rightarrow 2NO_2^- \quad (13)$$

The first oxidation step appears irreversible at scan rates 50−200 mV/s, because there is no associated cathodic peak when the potential scan is reversed after the first oxidation wave (Figure S5).

The second anodic peak at ∼4.00 V and the third anodic peak at ∼4.16 V vs Li^+/Li were both assigned to NO oxidation according to reaction 12. CV of $NOBF_4$ in AN solution showed that the NO/NO^+ couple is quasi-reversible, with a midpoint potential of 4.05 V (Figure S4). However, when $LiNO_3$ was incrementally added to solution of $NOBF_4$, a peak splitting similar to the one shown in Figure 5 was observed (see Supporting Information and Figure S6 for more details). We offer the following interpretation of this phenomenon. First we note that the first anodic wave for NO oxidation in the presence of NO_2^- and NO_3^- is slightly shifted to a less positive potential (by ∼0.05 V). This observation can be rationalized by considering a fast transformation of electrogenerated NO^+ according to reactions 10 and 11. The *in situ* generated NO_2 dimer can subsequently react with NO_2^- to form NO_3^- and NO again. As a result, NO is being continuously generated during the second oxidation wave at ∼4.00 V, giving rise to the third anodic wave at ∼4.16 V vs Li^+/Li. Fast kinetics for the reaction of NO_3^- with the excess of NO^+ near the electrode surface can account for the absence of NO_3^- oxidation peak at ∼4.95 V. The two small successive cathodic waves at ∼4.05 and ∼3.46 V were attributed to the reduction of NO^+ and NO_2/N_2O_4, respectively.

The nonlinear fitting procedure implemented in DigiElch[43] was used to establish the set of simulation parameters that provides the best average agreement between simulation and experiment at various scan rates (Table S3). The points in Figure 5a represent the best-fit simulation voltammograms based on reactions 9−12. We note that it was not possible to obtain a satisfactory fit to the experimental CVs by using the overall reaction 4 directly (as opposed to using reactions 10 and 11). This is consistent with quantum chemical calculations demonstrating a complex multistep mechanism for reaction 4 in AN solvent.

It is important to note that our calculations reproduce the anodic peak splitting with a single electrochemical step (reaction 12), which lends further credit to our mechanistic interpretation of NO oxidation in CV experiments. Sensitivity analysis of simulation parameters further reveals that the NO/NO^+ peak splitting can only be observed if the diffusion coefficients of NO and NO_2 and the rate constant for reaction 10 are above a certain threshold, while the diffusion coefficient of NO_3^- is below a certain limit. This could explain why the peak splitting is observed in some solvents[16,19] but not in others.[12,22]

Although a reasonable fit between simulated and experimental CVs was obtained in Figure 5a, some notable discrepancies are evident. The simulation significantly underestimates the height of the cathodic peak at ∼3.46 V and does not reproduce the relative heights of the second and third anodic waves as the scan rate increases. Additionally, the cathodic current at 3.8−4.0 V drops and rises more quickly than indicated by experiment. Theoretical calculations established (Section 4.5) that the autodissociation process is more complex than that described by reaction 10. To determine if the additional reactions predicted by the theory improve the agreement between simulations and the experimental voltammograms, a more comprehensive reaction scheme was employed in the simulations (model 2), which in addition to reactions 9, 11, and 12 includes the following steps:

$$NO_2 + NO_2 \rightleftharpoons N_2O_4 \quad (14)$$

$$NO_2 + NO_2 \rightleftharpoons \textit{trans}\text{-ONO-}NO_2 \quad (15)$$

$$\textit{trans}\text{-ONO-}NO_2 \rightleftharpoons NO^+ + NO_3^- \quad (16)$$

$$NO_2 + NO \rightleftharpoons N_2O_3 \quad (17)$$

$$\textit{trans}\text{-ONO-}NO_2 + e \rightarrow NO + NO_3^- \quad (18)$$

$$N_2O_4 + e \rightarrow NO + NO_3^- \quad (19)$$

As evident from Figure 5b, the inclusion of a more complete set of reactions provides significant improvements to the fits. The equilibrium constants for reactions 11 and 14−17 used in the simulation (Table S3) are in good agreement with the calculated reaction free energies in AN. The high rates of reactions 15 and 16 used in the simulation are consistent with the relatively low barriers of these reactions estimated from theoretical calculations (Figure 4). Furthermore, the ratio of diffusion coefficients, D_{NO2}/D_{NO2^-} and $D_{NO}/D_{NO^+} < 1$, found by simulation (Table S2) is in line with the increase of the effective hydrodynamic radius for the stronger solvated ionic species compared to the neutral counterpart.[49] It should be emphasized that all of the above reactions provide incremental improvements in the quality of the fit. The inclusion of N_2O_3 (reaction 17) was motivated by the increased stability of this oxide in aprotic organic solvents, such as AN.[50] The addition of electrode reactions 18 and 19 was needed in order to adequately reproduce the cathodic part of the CVs. Thus, the results demonstrate that quantum chemical calculations provide a useful framework to identify the intermediate products responsible for voltammetric behavior of nitrite ions under Ar in AN solution.

The proposed mechanism for the oxidation of $LiNO_2$ under Ar can be extended to describe the electrochemical behavior of $LiNO_2$ in the presence of oxygen by considering a fast reaction[51] between NO and O_2

$$NO + 1/2O_2 \rightarrow NO_2 \quad (20)$$

NO generated at the first oxidation wave, according to the overall reaction 13, is quickly converted[51] to NO_2, which in turn rapidly reacts with NO_2^- (the overall reaction 4) to create a catalytic loop where more NO is produced to react again with O_2. Taking the reactions steps 4, 13, and 20 together, the overall process can be summarized as follows

$$nNO_2^- + (n-1)/2O_2 \rightarrow (n-1)NO_3^- + NO_2 + e \quad (21)$$

where n depends on the relative rates of the chemical and electrochemical steps. The changes in first-scan voltammograms of 10 mM $LiNO_2$ in AN observed upon switching from Ar to O_2 atmosphere are fully consistent with this mechanistic picture (Figure 6).

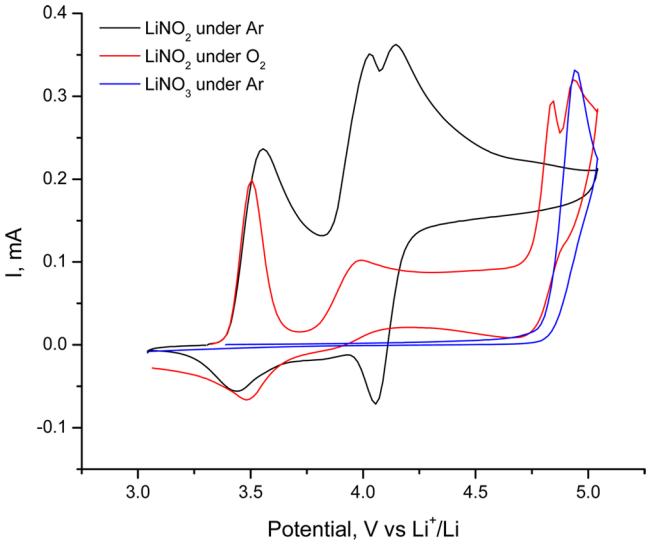

Figure 6. IR-corrected first scan cyclic voltammograms for the oxidation of 10 mM $LiNO_2$ under argon (black curve) and oxygen (red curve) and oxidation of 10 mM $LiNO_3$ under Ar (blue curve) in 0.5 M LiTFSI/AN electrolyte on a Pt macroelectrode (surface area = 0.196 cm^2) at a scan rate of 100 mV/s.

Indeed, the first anodic peak current is considerably lower under O_2, because the consumption of NO_2^- via anodic oxidation competes with consumption resulting from the chemical reaction in the presence of O_2. In addition, two new peaks at ~4.85 and ~4.95 V vs Li^+/Li are generated in the voltammogram under O_2. The first peak at ~4.85 V appears in the same potential range where the oxidation of NO_2 to NO_2^+ occurs (as evidenced both by measurements[21] and calculations given in Table 4). The second peak at ~4.95 V is unequivocally attributed to the oxidation of NO_3^-, as shown by the direct comparison with the anodic peak for the oxidation of 10 mM $LiNO_3$ in AN (Figure 6). Finally, we note that the first anodic peak at ~3.5 V completely disappears under steady-state conditions, indicating a full conversion of NO_2^- according to process (reaction 21) near the electrode surface. This provides a mechanism by which NO_3^- can at least be partially regenerated from NO_2^- under conditions that are uniquely possible in Li-O_2 cells during the process of cell charging. Preventing or mitigating the loss of $LiNO_3$ served to stabilize the SEI on Li metal (reaction 1) could be a contributing factor to the observed synergistic effect of O_2 and $LiNO_3$ on the interfacial stability and cycling of Li metal, as reported[11] by our group previously.

5. CONCLUSIONS

Degradation of electrolyte components under conditions that exist in rechargeable Li-O_2 batteries is one of the most difficult challenges to overcome. Recently we have presented a new strategy for stabilizing the Li/electrolyte interface in solvents that do not form a stable SEI on their own.[6,11] $LiNO_3$ was found to serve the dual purpose of an electrolyte salt and an SEI film stabilizing agent. The reduction of $LiNO_3$ on the Li metal results in the formation of insoluble Li_2O that contributes toward stabilizing the SEI film, while the other more soluble product, $LiNO_2$, is electroactive within the operating potential window of a Li-O_2 cell.[6] Due to lack of detailed mechanistic understanding of nitrite oxidation, there are significant contradictions and variations in the interpretation of the successive oxidation waves of the nitrite anion. In this work we apply first-principles computational methods to understand the chemical and electrochemical behavior of $LiNO_2$ in AN and identify the intermediate products responsible for voltammetric behavior of nitrite ion in AN solution. Our computational protocol based on coupled-cluster calculations at the complete basis set limit (RCCSD(T)/CBS) in the gas phase and mixed cluster/continuum calculations is solution is capable of accurately predicting the redox potentials of oxygenated nitrogen compounds in AN. A detailed analysis of reaction between NO_2^- and NO_2/N_2O_4 suggests a mechanism in which the interconversion between nitrogen dioxide and its various dimers provides a low-energy path for the reaction with the nitrite anion. A set of coupled electrochemical and chemical steps predicted by the theory was used to build the reaction network for the digital simulation of cyclic voltammograms of $LiNO_2$ in AN under argon. Good agreement between simulations and the experimental voltammograms is only achieved with inclusion of a more complete set of reactions suggested by the theory. The results establish a possible mechanism of regeneration of $LiNO_3$ in electrolyte in the presence of oxygen, which is uniquely possible under charging conditions in a Li-O_2 battery.

In a more broad content, this study provides a theoretical framework for computational electrochemistry in solution. We find that with a choice of an accurate computational method in the gas phase, implicit solvation model optimized for neutral molecules, and explicit consideration of the most important solute−solvent interactions to describe the solvation of ions, first principles methods can provide valuable insights into mechanisms of electrochemical processes in organic media and guide the assignment of the cyclic voltammetry peaks.

■ ASSOCIATED CONTENT

Supporting Information

Complete ref 26, RMP2 and RCCSD(T) reaction/activation energies as a function of basis set size (Table S1), performance of several DFT methods in reproducing the redox potentials of oxygenated nitrogen compounds (Table S2), parameters employed in the CV simulation of NO_2^- oxidation under Ar (Table S3), additional computational (Figures S1, S2) and experimental details (Table S4, Figures S3−S6), Cartesian coordinates, electronic states, and absolute energies (in Hartrees) for tested molecular structures obtained with the B3LYP functional. This material is available free of charge via the Internet at http://pubs.acs.org.

■ AUTHOR INFORMATION

Corresponding Author

slava@liox.com

Notes

The authors declare no competing financial interest.

■ REFERENCES

(1) Girishkumar, G.; McCloskey, B.; Luntz, A. C.; Swanson, S.; Wilcke, W. J. *J. Phys. Chem. Lett.* **2010**, *1*, 2193−2203.
(2) Bruce, P. G.; Freunberger, S. A.; Hardwick, L. J.; Tarascon, J.-M. *Nat. Mater.* **2012**, *12*, 19−29.
(3) Christensen, J.; Albertus, P.; Sanchez-Carrera, R. S.; Lohmann, T.; Kozinsky, B.; Liedtke, R.; Ahmed, J.; Kojic, A. *J. Electrochem. Soc.* **2012**, *159*, R1−R30.
(4) Shao, Y.; Ding, F.; Xiao, J.; Zhang, J.; Xu, W.; Park, S.; Zhang, J.-G.; Wang, Y.; Liu, J. *Adv. Funct. Mater.* **2013**, *23*, 987−1004.

(5) Cheng, F.; Chen, J. *Chem. Soc. Rev.* **2012**, *41*, 2172−2192.
(6) Walker, W.; Giordani, V.; Uddin, J.; Bryantsev, V. S.; Chase, G. V.; Addison, D. A. *J. Am. Chem. Soc.* **2013**, *135*, 2076−2079.
(7) Bryantsev, V. S.; Uddin, J.; Giordani, V.; Walker, W.; Addison, D.; Chase, G. V. *J. Electrochem. Soc.* **2013**, *160*, A160−A171.
(8) Poris, J.; Raistrick, I.; Huggins, R. *Proc. Electrochem. Soc.* **1984**, *84*−*2*, 313−321.
(9) Aurbach, D.; Pollak, E.; Elazari, R.; Salitra, G.; Kelley, C.; Affinito, J. *J. Electrochem. Soc.* **2009**, *156*, A694−A702.
(10) Zhang, S. S. *Electrochim. Acta* **2012**, *70*, 344−348.
(11) Giordani, V.; Walker, W.; Bryantsev, V. S.; Uddin, J.; Chase, G. V.; Addison, D. A. *J. Electrochem. Soc.* **2013**, *160*, A1544−A1550.
(12) Uddin, J.; Bryantsev, V. S.; Giordani, V.; Walker, W.; Chase, G. V.; Addison, D. A. *J. Phys. Chem. Lett.* **2013**, *4*, 3760−3765.
(13) Martins, M. E.; Calandra, A. J.; Arvía, A. J. *Electrochim. Acta* **1970**, *15*, 111−126.
(14) Castellano, C. E.; Wargon, J. A.; Arvía, A. J. *Electroanal. Chem. Interfacial Electrochem.* **1973**, *47*, 371−372.
(15) Bontempelli, G.; Mazzocchin, G.-A.; Magno, F. *Electroanal. Chem. Interfacial Electrochem.* **1974**, *55*, 91−100.
(16) Bontempelli, G.; Mazzocchin, G.-A.; Magno, F.; Seeber, R. *Electroanal. Chem. Interfacial Electrochem.* **1974**, *55*, 101−107.
(17) Lee, K. Y.; Kuchynka, D. J.; Kochi, J. K. *Inorg. Chem.* **1990**, *29*, 4196−4204.
(18) Lee, K. Y.; Amatore, C.; Kochi, J. K. *J. Phys. Chem.* **1991**, *95*, 1285−1294.
(19) Boughriet, A.; Fischer, J. C.; Leman, G.; Wartel, M. *Bull. Soc. Chim. Fr.* **1985**, *1*, 8−13.
(20) Boughriet, A.; Coumare, A.; Wartel, M. *Electrochim. Acta* **1990**, *35*, 389−397.
(21) Boughriet, A.; Wartel, M. *J. Electroanal. Chem.* **1993**, *362*, 167−176.
(22) Broder, T. L.; Silvester, D. S.; Aldous, L.; Hardacre, C.; Compton, R. G. *J. Phys. Chem. B* **2007**, *111*, 7778−7785.
(23) Bryantsev, V. S.; Diallo, M. S.; Goddard, W. A., III *J. Phys. Chem. B* **2008**, *112*, 9709−9719.
(24) Bryantsev, V. S. *Theor. Chem. Acc* . **2012**, *131*, 1250−1−7.
(25) Möller, C.; Plesset, M. S. *Phys. Rev.* **1934**, *46*, 618−622.
(26) Straatsma, T. P.; Aprà, E.; Windus, T. L.; Bylaska, E. J.; de Jong, W.; Hirata, S.; Valiev, M.; Hackler, M.; Pollack, L.; Harrison, R. et al. *NWChem, A Computational Chemistry Package for Parallel Computers*, version 5.1; Pacific Northwest National Laboratory, Richland, WA, 2007.
(27) Purvis, G. D., III; Bartlett, R. J. *J. Chem. Phys.* **1982**, *76*, 1910−1918.
(28) Raghavachari, K.; Trucks, G. W.; Pople, J. A.; Head-Gordon, M. *Chem. Phys. Lett.* **1989**, *157*, 479−483.
(29) Watts, J. D.; Gauss, J.; Bartlett, R. J. *J. Chem. Phys.* **1993**, *98*, 8718−8733.
(30) Dunning, T. H., Jr. *J. Chem. Phys.* **1989**, *90*, 1007−1023.
(31) Kendall, R. A.; Dunning, T. H., Jr.; Harrison, R. J. *J. Chem. Phys.* **1992**, *96*, 6796−6806.
(32) Koch, H.; Fernandez, B.; Christiansen, O. *J. Chem. Phys.* **1998**, *108*, 2784−1−7.
(33) Liu, W.-G.; Goddard, W. A., III. *J. Am. Chem. Soc.* **2012**, *134*, 12970−12978.
(34) Becke, A. D. *Phys. Rev. A* **1988**, *38*, 3098−3100.
(35) Lee, C. T.; Yang, W. T.; Parr, R. G. *Phys. Rev. B* **1988**, *37*, 785−789.
(36) Zhao, Y.; Truhlar, D. G. A *J. Chem. Phys.* **2006**, *125*, 194101−1−17.
(37) Zhao, Y.; Truhlar, D. G. *Theor. Chem. Acc* . **2008**, *120*, 215−241.
(38) *Jaguar*, version 7.7, Schrödinger, LLC, New York, 2010.
(39) Ribeiro, R. F.; Marenich, A. V.; Cramer, C. J.; Truhlar, D. G. *J. Phys. Chem. B* **2011**, *115*, 14556−14562.
(40) Boughriet, A.; Wartel, M.; Fischer, J. C. *J. Electroanal. Chem.* **1985**, *190*, 103−115.
(41) Blanco, M. *J. Comput. Chem.* **1991**, *12*, 237−247.
(42) Fan, C. F.; Olafson, B. D.; Blanco, M.; Hsu, S. L. *Macromolecules* **1992**, *25*, 3667−3676.
(43) Rudolph, M. *J. Comput. Chem.* **2005**, *26*, 1193−1204; see also www.ElchSoft.com.
(44) Feller, D.; Dixon, D. A. *J. Chem. Phys.* **2001**, *115*, 3484−1−13.
(45) Řezáč, J.; Hobza, P. *J. Chem. Theory Comput.* **2013**, *9*, 2151−2155.
(46) *NIST Chemistry Webbook*; NIST: Gaithersburg, MD, 2005, http://webbook.nist.gov/chemistry/
(47) Kelly, C. P.; Cramer, C. J.; Truhlar, D. G. *J. Phys. Chem. B* **2007**, *111*, 408−422.
(48) Bryantsev, V. S.; Addison, D.; Chase, G. V. *J. Electrochem. Soc.* **2013**, *160*, H818−H819.
(49) Macías-Ruvalcaba, N. A.; Evans, D. H. *J. Phys. Chem. B* **2010**, *114*, 1285−1292.
(50) Boughriet, A.; Wartel, M.; Fischer, J. C.; Auger, Y. *J. Electroanal. Chem.* **1985**, *186*, 201−209.
(51) Gary, R. M. *Synthetic Nitrogen Products: A Practical Guide to the Products and Processes*; Kluwer Academic/Plenum Publishers: New York, 2004.